# Effect of heat treatment time on the transport properties of nano-crystallized Li$_2$O–Na$_2$O–V$_2$S$_5$–P$_2$S$_5$ glass–ceramics

A. M. Al-Syadi[1,2] · M. Abaker[1,2]

## Abstract

The structural and electrical characteristics of the glassy system with the chemical formula (18.75Li$_2$O–18.75Na$_2$O–25V$_2$S$_5$–37.5P$_2$S$_5$ mol%) and its nano-crystallized glass–ceramics have been investigated. The glass sample was prepared via the conventional melt-quenching technique. The corresponding nano-crystallized glass–ceramics were prepared via a heat treatment (HT) procedure at 405 °C for diverse times in the air. The effect of HT time on nanostructure and the dc conductivity for the nano-crystallized glass–ceramics were investigated. X-ray diffraction (XRD) spectra and field emission scanning electron microscopy (FESEM) images confirmed the amorphous nature of the as-synthesized glass and the growth of nano-crystals after heat treatment within the glassy matrix. The nano-crystallized glass–ceramics exhibited considerably higher conductivity and lower activation energy than the initial glass. Furthermore, the dc conductivity was improved by nearly 57 times in the nano-crystallized glass–ceramic samples as compared with the initial glass. The activation energy was improved by utilizing the HT process and was found to be 0.535 eV for the as-prepared glass and between 0.272 and 0.462 eV for the corresponding nano-crystallized glass–ceramics. The dc conductivity increased with decreasing crystalline size in the case of nano-crystallized glass–ceramics, which may be accredited to the reduction in grain boundary scattering brought on by the smaller particle size. The conduction mechanism was emphasized to follow the non-adiabatic small polaron hopping (SPH).

**Keywords** Vanadium phosphorus sulfide glass · Nano-crystallized glass–ceramic · Dc conductivity · Transport properties · Small polaron hopping

## 1 Introduction

Glasses and nano-crystallized glass–ceramics containing transition metal ions (TMIs), like Fe, V, Co, and W, are of tremendous interest owing to their possible applications [1–6]. They display semiconducting properties because of the existence of two diverse valance states of the TMIs, for instance, V$^{4+}$ and V$^{5+}$ in the case of vanadium or Fe$^{2+}$ and Fe$^{3+}$ in the case of iron. This charge transmission is commonly named SPH, in which the small polaron jumps from the low to the high valence state, and occurs electron conduction in the glasses [3–6]. Alkali phosphate glass, doped with TMI (such as V), is of considerable interest owing to its attractive optical, semiconductor, electrical, and thermal characteristics and their particular applications. Recently, this category of materials has made interesting candidates in several fields of application such as mechanical and thermal sensors, reflecting windows, optical filters, ray absorbers, non-linear optical and electronic devices, switching, memory elements, and batteries materials [7–12]. In the latest decades, glass–ceramics relying on alkali phosphate has been effectively optimized by a crystallization handling of the initial glass, and the conductivity of alkali ions has been investigated [7, 10–12]. The crystallization of glass is a technique to manufacture nano-materials and it is remarkable to optimize novel conductive materials with these nanostructures [7, 10–12]. In the glass–ceramic technique, it is conceivable to prepare the desired crystalline phase from the homogeneous glassy stage and to produce the size and form of the crystalline stage by controlled crystal nucleation

✉ A. M. Al-Syadi
arefalsyadi@yahoo.com; amalsyadi@nu.edu.sa

M. Abaker
meabaker@nu.edu.sa

1   Department of Physics, Faculty of Science and Arts, Najran University, Najran, Saudi Arabia

2   Promising Centre for Sensors and Electronic Devices (PCSED), Advanced Materials and Nano-Research Centre, Najran University, Najran, Saudi Arabia

and growth. Alkali ions modifiers are expected to inhabit non-bridging oxygen (NBO) sites in the glass phase [9–11]. This means the addition of alkali oxides such as $Li_2O$ and $Na_2O$ to the glassy matrix results in structural changes by the opening up of the glass network as NBO increases, thereby causing higher ionic conductivity and hence increasing electrical conductivity [13]. The applications of these glasses and corresponding nano-crystallized glass ceramics have also obtained increased attention owing to their possible use as electrodes in solid-state devices [13]. Heat treatment of the glassy stage nearby their crystallization temperature for diverse times fabricates nano-crystals entrenched in the specimens. The nano-crystalline phase is very important to enhance numerous properties, such as the electrical conductivity of the glass [10–12, 14–19]. Moreover, the alkali phosphate glass containing vanadium yields mixed ionic and electronic conductivity happening through the transport of electron hopping and alkali ions between vanadium ions centers [6, 11, 20]. However, the existence of sulfur in the glassy matrix leads to improve electrical conductivity. The attendance of S ions can enlarge the size of alkali ion transport passageways due to the larger diameters of S ions than O ions. In addition to that, the S ions have a high polarization aptitude than O ions, which leads to a weakening of the bond between alkali ions ($Li^+$ and $Na^+$) and the skeleton [21]. Moreover, the S atoms work as a reduction agent that reasons decreasing V ions from the higher to the lower valence states [6, 10]. This decrease is important to get compounds containing $V^{3+}$ and $V^{4+}$, consequently can boost electrical characteristics via easiness of the electrons and ions transmission [6, 11, 22]. Moreover, the electrochemical performance of energy storage devices (batteries or supercapacitors) depends greatly on the electrical conductivity of the electrode materials [23, 24], which makes the study of this conductivity very important.

In this study, the $Li_2O–Na_2O–V_2S_5–P_2S_5$ glass and its nano-crystallized glass–ceramics are synthesized. The improvement of the electrical conductivity due to the existence of the nano-crystalline phases inside the glassy matrix is investigated as a function of crystalline size. In addition, the mechanism of electrical conductivity of the as-synthesized glass and nano-crystallized glass–ceramics is clarified.

## 2 Experimental work

The glassy system with the chemical formula ($18.75Li_2O–18.75Na_2O–25V_2S_5–37.5P_2S_5$ mol%) was fabricated through the conventional melt-quenching technique. The corresponding nano-crystallized glass–ceramics were manufactured through the HT process of the glassy sample via annealing in the midair at 405 °C for 2, 5, 10, and 20 h. Further details concerning the glass and corresponding nano-crystallized

glass–ceramics synthesis were given in our previous paper Ref. [11]. The density values of the glassy specimen and corresponding nano-crystallized glass–ceramics were scaled using the Archimedes technique in Toluene as a dipping liquid ($d_{(Toluene)} = 0.8669$ g/cm³). XRD $2\theta$ scans were carried out to examine the glassy/nano-crystalline phases in the prepared samples by utilizing a Panalytical X'pert Pro diffractometer. FESEM; JSM-7600F-JEOL) was utilized to study the surface morphology of samples. For dc conductivity measurements, bulk samples were highly polished and then coated with silver paste on both surfaces of the pellet. The dc conductivity values were estimated by both current and voltage values by applying a constant dc voltage of 2 V to the pellets at room temperature (RT).

## 3 Results and discussion

### 3.1 Characterization of glass and nano-crystallized glass–ceramics

Figure 1 displays the XRD spectra of the as-synthesized glass sample and nano-crystallized glass–ceramics annealing at 450 °C, after the crystallization temperature ($T_c$) that was obtained from differential scanning calorimetry (DSC) as reported in our preceding work [25], for varied times (2, 5, 10, and 20 h). This figure exhibits the XRD of amorphous, Fig. 1a, and partially crystalline samples, Fig. 1b. It can be noticed that the glassy sample exhibited an amorphous halo exemplar for glass. The corresponding nano-crystallized glass–ceramics exhibited sharp reflections of diverse crystalline phases. The intensity and width of the reflections changed with diverse heat-treating times from 2 to 20 h. These crystalline phases indicated the structures of $P_4S_5$ (JCPDS#00-010-0329), $Li_4P_2S_6$ (JCPDS#01-076-0992), $Na_2O$ (JCPDS#00-002-1288) and $Li_3VO_4$ (JCPDS#00-013-0249) [11, 25]. These nano-crystalline phases were different compared to the phases that were obtained in the previous papers [6, 26]. This may be due to the presence of mixed alkali oxides ($Li_2O$ and $Na_2O$) and using $P_2S_5$ and $V_2S_5$ instead of $P_2O_5$ and $V_2O_5$. The crystalline size ($D$) of the nano-crystallized glass–ceramics was calculated by the full width at half maximum (FWHM) of the most intense peaks based on the average value of the several crystalline phases using the following equation [26]:

$$D = \frac{c\lambda}{\beta\cos\theta} + 2\varepsilon\sin\theta, \qquad (1)$$

where $c \approx 0.9$, $\lambda = 0.15406$ nm is the wavelength of X-ray used, $\beta$ is the FWHM in radians, $\epsilon$ is the lattice strain, and $\theta$ is the Bragg angle. The $\epsilon$ in powders because of crystal
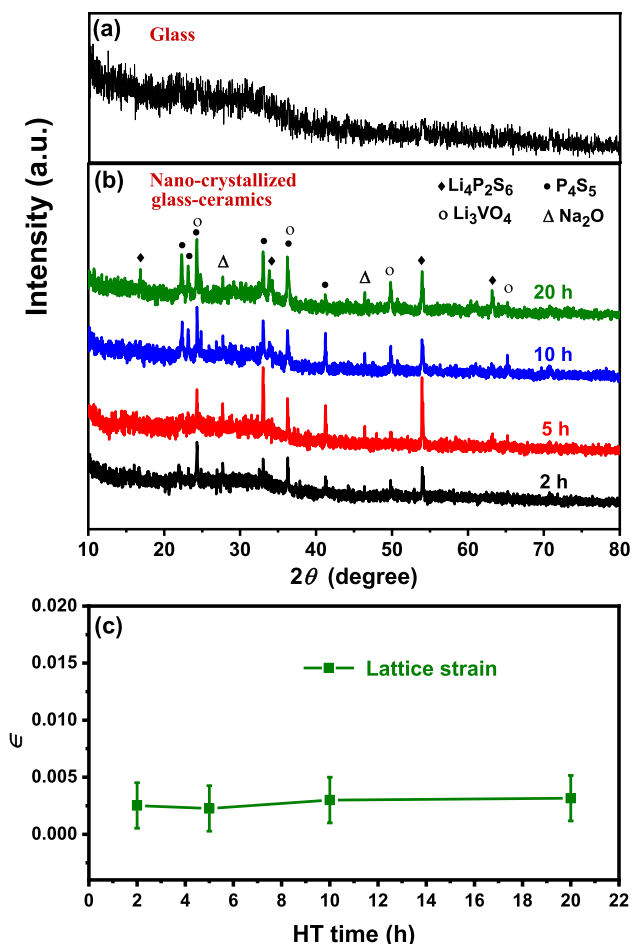
**Fig. 1** XRD for **a** the as-synthesized glass; **b** nano-crystallized glass–ceramics at diverse HT times; **c** effect of HT time on lattice strain ($\epsilon$) for nano-crystallized glass–ceramics

distortion and crystal defect was estimated by utilizing the formula [26, 27]:

$$\epsilon = \frac{\beta}{4\tan\theta}. \tag{2}$$

The $D$ values for nano-crystallized glass–ceramics were obtained to be between 37 and 50 nm, as recorded in Table 1. These outcomes agree with the outcomes achieved by transmission electron microscopy (TEM) images reported in our previous work [11]. It is found that when the annealing time raised from 2 to 5 h, the $D$ raised from 47 to 50 nm, respectively. After that, when the annealing time was raised to 10 h and 20 h, the $D$ reduced to 42 nm and 37 nm, respectively. This result could be explained as follows: first, the heat-treating of the glass sample led to an increase in the atomic movement and boosted the capability of atoms to get the actively preferred sites and therefore the crystalline size increased with increasing HT time. Then, the increase in heat treatment time introduced many defects in the crystalline phase which destroyed the long-range clustering, causing the reduction of the crystal size [28, 29]. The variation of $\epsilon$ values for the as-synthesized nano-crystallized glass–ceramics with the difference in annealing time was displayed in Fig. 1c. The lattice strain of these nano-crystallized glass–ceramics was nearly similar ($\approx 0.003$), proposing that the lattice of the crystallite phase was not deformed with differences of $D$ in the obtained crystalline phases (i.e., the as-synthesized nano-crystallized glass–ceramics had similar lattice constructions by variation of $D$ in the obtained crystalline phases) [26, 30].

Figure 2 shows the FESEM images of the glass sample and nano-crystallized glass–ceramic annealing for 10 h. For the glassy sample, Fig. 2a, there are no discernible crystals, demonstrating an amorphous phase feature. The nano-crystallized glass–ceramic sample, Fig. 2b, on the other hand, had big secondary particles resulting from an aggregation of small elementary grains, and they did not have a regular form. The transport properties of nano-crystallized glass–ceramics are influenced by these grains. It is possible that the intrinsic features, such as conductivity, are responsible for the enhanced dynamics of alkali (such as Na and Li) ions, electrical properties, and electrochemical properties of these samples. Alkali ions do not disperse over a longer distance between the surface and the core during alkali transportation in grains with a relatively high surface area [11, 26]. This outcome showed that annealing may produce a comparatively large surface area, leading to elevated electronic and ionic conductivity, bigger capacity, and the highest rate ability [11, 16, 26]. As a result, these composites may be appropriate materials for use as electrodes in energy storage devices that need strong electronic and ionic conductivity (such as batteries or supercapacitors).

**Table 1** Crystalline size ($D$), density ($d$), Oxygen packing density (OPD) and physical properties of 18.75Li₂O–18.75Na₂O–25V₂S₅–37.5P₂S₅ glass and its nano-crystallized glass–ceramics at diverse HT times

| Sample | $D \pm 1$ (nm) | $d \pm 0.02$ (g cm$^{-3}$) | $V_m \pm 0.02$ (cm$^3$ mol$^{-1}$) | $N \times 10^{22}$ (cm$^{-3}$) | $R$ (nm) | $W \pm 0.001$ (eV) | $\Theta_D \pm 2$ (K) | $\nu_0 \pm 0.001$ ($\times 10^{13}$ Hz) |
|---|---|---|---|---|---|---|---|---|
| Glass | – | 2.58 | 42.57 | 1.186 | 0.439 | 0.535 | 654 | 1.362 |
| HT 2 h | 47 | 3.06 | 35.87 | 1.407 | 0.414 | 0.415 | 694 | 1.445 |
| HT 5 h | 50 | 3.23 | 34.04 | 1.483 | 0.407 | 0.462 | 678 | 1.412 |
| HT 10 h | 42 | 2.80 | 39.31 | 1.284 | 0.427 | 0.339 | 698 | 1.454 |
| HT 20 h | 37 | 2.62 | 41.96 | 1.203 | 0.436 | 0.272 | 722 | 1.504 |
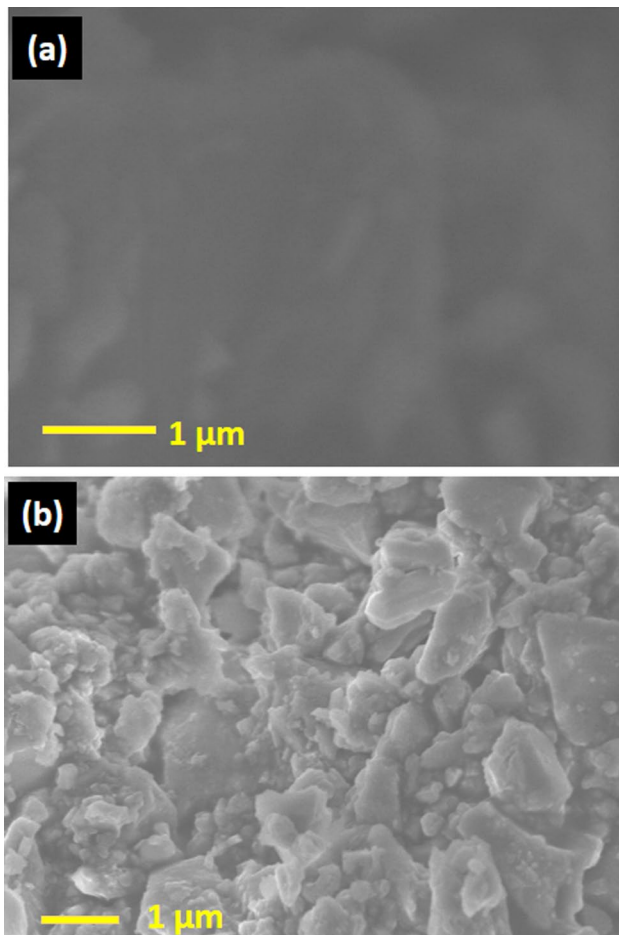
Fig. 2 SEM for **a** the glass sample; **b** nano-crystallized glass–ceramic annealing at 405 °C for 10 h



Fig. 3 The relation between $d$ and $V_m$ with the change of HT time for the glass sample and nano-crystallized glass–ceramics

## 3.2 Density and molar volume

Utilizing toluene as a dipping liquid, Archimedes' principle was used to compute the density ($d$) of the current glass and nano-crystallized glass–ceramics. The $d$ values are scheduled in Table 1. The $d$ of the glass sample was 2.58 g/cm³. However, the $d$ values of nano-crystallized glass–ceramics were between 2.62 and 3.23 g/cm³. It was found that the densities of nano-crystallized glass–ceramics were greater than that of glass. The rise in density of nano-crystallized glass–ceramics might be owing to molecular rearrangement, which caused structural alterations. That is, the structure in nano-crystallized glass–ceramics was more tightly packed than in the comparable glass phase [31, 32]. As demonstrated in Table 1, for the nano-crystallized glass–ceramics, the $d$ values followed the same crystalline size behavior with HT time, i.e., the variation in $d$ values was owing to changes in the crystalline size caused by variations in the volume of these crystallite phases [6]. Table 1 shows that the magnitude of density was highest in nano-crystallized
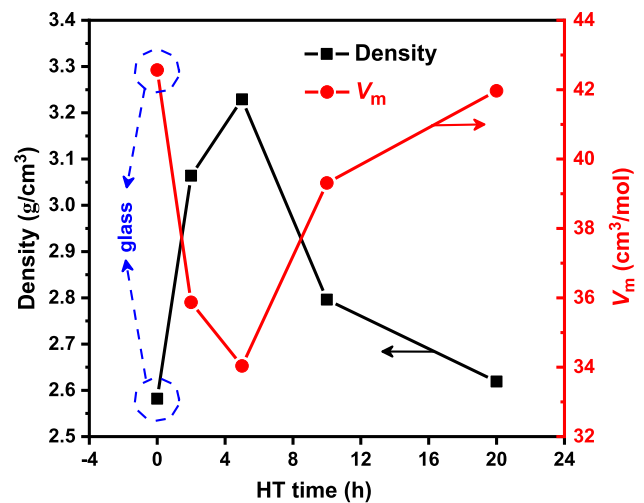
glass–ceramics with the biggest crystalline size, which is consistent with prior research [6, 16, 33]. For all samples, the molar volume ($V_m$) was computed using the formula [34]:

$$V_m = \frac{M}{d},\tag{3}$$

where $M$ is molecular weight and $d$ is density, respectively. The $V_m$ of glass and corresponding nano-crystallized glass–ceramics are scheduled in Table 1. The relation between $d$ and $V_m$ with the change of HT time is displayed in Fig. 3. Since $d$ is related to the mean molecular weight that is oppositely proportional to $V_m$, it is usually anticipated that $d$ and $V_m$ must display an inverse proportion [32].

## 3.3 DC conductivity

The reciprocal temperature reliance of the dc conductivity ($\sigma_{dc}$) for the as-prepared glass and corresponding nano-crystallized glass–ceramics that measured between 313 and 473 K was illustrated in Fig. 4. The figure displays that the chart became a straight line above a specified temperature, $\theta_D/2$, where $\theta_D$ is the Debye temperature (listed in Table 1), suggesting that the $\sigma_{dc}$ follows the Arrhenius relation [34]:

$$\sigma_{dc} = \sigma_0 \exp\left(\frac{-W}{kT}\right),\tag{4}$$

where $k$ is the Boltzmann constant, $W$ is the activation energy for conduction, and $\sigma_0$ is the preexponential factor matching electrical conductivity at high temperatures. $W$ is necessary to overawe the energy barriers and electrostatic force throughout the leap. Thus, as could be shown
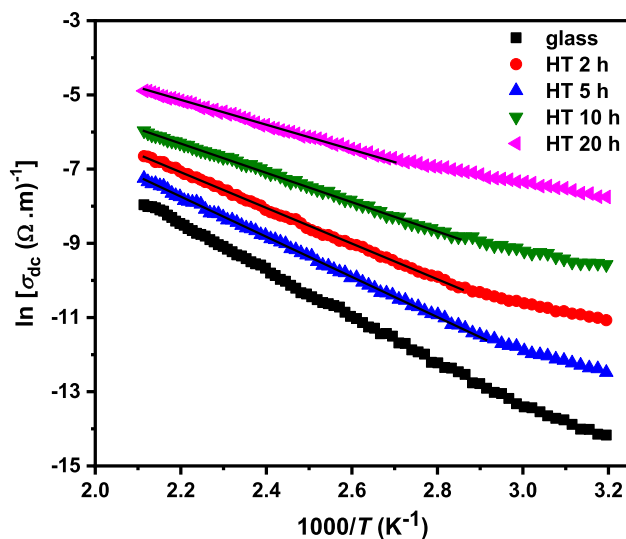
**Fig. 4** Reciprocal temperature reliance of the $\sigma_{dc}$ for the glass sample and nano-crystallized glass–ceramics



**Fig. 5** Effect of HT time on $\sigma_{dc}$ at a specified temperature (409 K) and $D$ for the nano-crystallized glass–ceramics

in Fig. 4, the $\sigma_{dc}$ rose with temperature, which is a common feature of semiconducting glasses. Furthermore, the transportation is ascribed to electronic at low-temperature (i.e., $T < \theta_D/2$); however, Li and Na ions might be moveable and take part in the conduction process at the high-temperature area (i.e., $T > \theta_D/2$). Several phosphate glasses exhibiting TMI are comparable to this [35–37]. The slope of the plots (Fig. 4) was used to compute the $W$, but the intercept of the straight-line fits of the data was used to get the $\sigma_0$. $W$ values in the high-temperature areas are scheduled in Table 1. The $\sigma_{dc}$ values of nano-crystallized glass–ceramics were greater than initial glass (Fig. 4). The existence of nano-crystals with average crystalline size in the range of 37–50 nm as observed in XRD was considered to be responsible for the improved conductivity. Other studies have reported remarkable increases in conductivity with the existence of nanostructure [16, 32, 35, 36]. To explain the electrical conductivity enhancement during nano-crystallization and decrease during colossal crystallization it is useful to refer to the well-established core–shell model. Pietrzaka et al. [37] have discussed this model. For this model a grain consists of an inner completely crystalline "core" and an outer highly disordered, defective, and non-stoichiometric "shell" [37]. The same "core–shell" model can clarify the conductivity improvement produced by nano-crystallization. The overlapping and intersecting defective shells around crystalline cores can form a complicated system of paths for facilitated electron transport. The mechanism of electronic transport in vanadium oxides consists of SPH between aliovalent $V^{4+}$ and $V^{5+}$ sites. In the regions where the local concentration of the $V^{4+}$–$V^{5+}$ pairs is high, the conductivity is also high. Such a circumstance takes place inside and around the defective

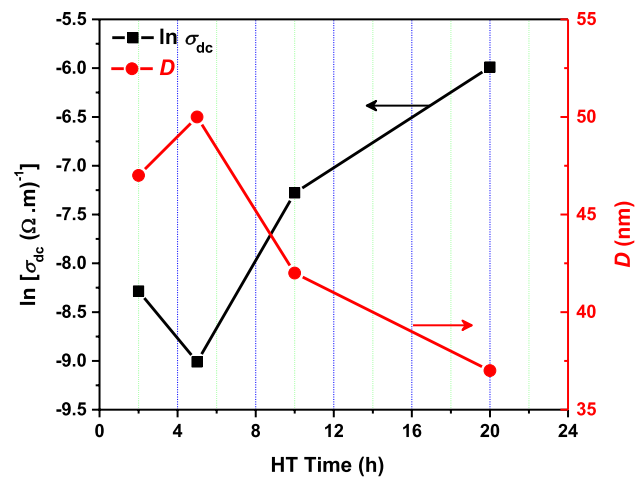grain-shell areas [37, 38]. In the case of colossal crystallization, the grains become well-developed crystallites with sharp edges. A negative result of this colossal crystallization is the decay of the "easy conduction paths" of the interfacial regions [37, 38]. However, the disappearance of the disordered shells due to colossal crystallization causes a considerable conductivity drop. On the other hand, heat-treated at 405 °C resulted in nanoparticles created in the glassy phase, which improved dc conductivity by forming a dense network of electrical conductivity routes between $V_2O_5$ nanoparticles [39]. Similar findings have recently been published in nano-crystallized glass–ceramics [16, 32]. Figure 5 depicts how changes in $\sigma_{dc}$ and crystalline size with the change in HT time. The $\sigma_{dc}$ and crystalline size clearly behaved in opposing manners. This suggests that grain boundary scattering had an influence on electrical conductivity. A potential barrier was created by the grain boundaries acting as electron traps. Conduction electrons scatter along grain boundaries as a result of the development of a potential barrier, reducing conductivity. As a result, the reduction in the scattering of grain boundary owing to decreasing crystalline size may be linked to the increase in conductivity [16, 32]. This result was in agreement with the results reported in previous works [6, 16, 28, 32, 35, 36, 38, 40]. With different HT times, the change in $\sigma_{dc}$ of the present glass and its nano-crystallized glass–ceramics at a specific temperature ($T = 409$ K°) and $W$ is shown in Fig. 6. According to Fig. 6, which conforms to the SPH conduction process in TMIs, the conductivity was lowest when the activation energy was higher. A conductivity of this nature results from the jumping of electrons between diverse valence states [34–37]. Consequently, the conductivity values at $T$ over $\theta_D/2$ were examined using the SPH model provided by Mott [41].
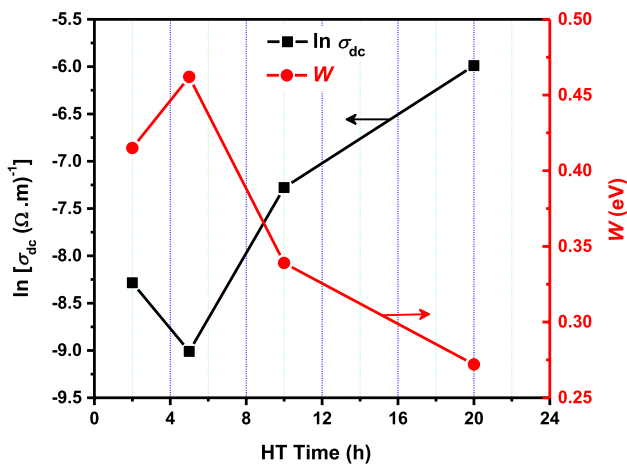
**Fig. 6** Influence of HT time on the $\sigma_{dc}$ (at 409 K) and $W$ for the nano-crystallized glass–ceramics

For the non-adiabatic system in the Mott model, the $\sigma_{dc}$ for jumping to the closest neighbor at $T > \theta_D/2$ was computed utilizing Eq. (4). The $\sigma_0$ in Eq. (4) was calculated by this formula [32]:

$$\sigma_0 = \frac{\nu_0 N e^2 R^2}{k} C(1 - C)\exp(-2\alpha R), \tag{5}$$

where $C$ is the fraction of TMI ($C = V^+/\sum V$), $N$ is the TMIs density, $R$ is the mean distance between TMIs, $\alpha$ is the tunneling factor, $e$ is the charge of the electron and the optical phonon frequency, denoted by the symbol $\nu_0$, is calculated using the formula ($k\theta_D = h\nu_0$, where h is Plank's constant). The values of $\nu_0$ were found to be between 1.362 and $1.504 \times 10^{13}$ Hz and are listed in Table 1.

The $W$ could be given as [32]

$$W = W_H + W_D/2 \text{ at } T > \theta_D/2, \tag{6}$$

$$W = W_D \text{ at } T < \theta_D/2, \tag{7}$$

where $W_p$ is the binding energy, $W_H$ is the polaron hopping energy $\left(W_H = W_P/2\right)$ and $W_D$ is the disorder energy that is defined as the variance in electronic energy between the

two hopping locations. The values of $W_D$ are summarized in Table 2.

The $\alpha R$ in Eq. (5) is insignificant in the adiabatic hopping system [32, 42], and the $\sigma_0$ is then described by the following formula [32, 34]:

$$\sigma_0 = \frac{\nu_0 N e^2 R^2}{k} C(1 - C). \tag{8}$$

The nature of the polaron hopping process might be ascertained from the graph of $\ln\sigma_{dc}$ versus $W$ at a constant experimental $T$ using the equation $\ln\sigma_{dc} = \ln\sigma_0 - W/2.303 k T_e$ (non-adiabatic or adiabatic) [6, 16, 42]. If the temperature ($T_e$) that is determined by the plot is close to $T$ then the hopping should take place in an adiabatic system. Otherwise, hopping will take place in a non-adiabatic system. Figure 7 illustrates the correlation between $\ln\sigma_{dc}$ and $W$ for nano-crystallized glass–ceramics at a constant temperature (409 K). The results were linear over the whole range of $W$ values, which was important to note. The $T_e$ was 323 K, which differed significantly from
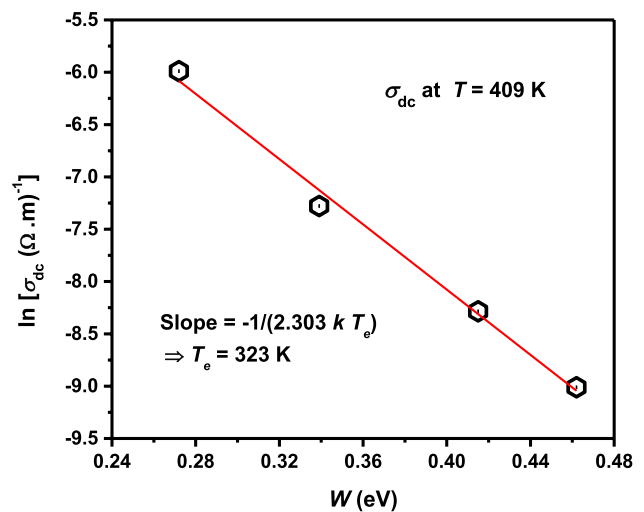


**Fig. 7** The correlation between $\ln\sigma_{dc}$ (at 409 K) and $W$ for the nano-crystallized glass–ceramics

**Table 2** SPH parameters of 18.75Li$_2$O–18.75Na$_2$O–25V$_2$S$_5$–37.5P$_2$S$_5$ glass and its nano-crystallized glass–ceramics at diverse HT times

| Sample | $W_H \pm 0.001$ (eV) | $W_D \pm 0.001$ (eV) | $r_p$ (nm) | $\varepsilon_p \pm 0.01$ | $N(E_F)$ ($\times 10^{21}$ eV$^{-1}$ cm$^{-3}$) | $\gamma_p \pm 0.01$ | $\ln\sigma_0 \pm 0.001$ ($\Omega^{-1}$ m$^{-1}$) | $\ln\sigma_{dc} \pm 0.02$ ($\Omega^{-1}$ m$^{-1}$) (at 409 K) |
|---|---|---|---|---|---|---|---|---|
| Glass | 0.354 | 0.362 | 0.177 | 43.11 | 5.295 | 12.56 | 5.178 | -10.03 |
| HT 2 h | 0.327 | 0.176 | 0.167 | 49.43 | 8.100 | 10.93 | 3.514 | -8.29 |
| HT 5 h | 0.375 | 0.175 | 0.164 | 43.91 | 7.668 | 12.81 | 4.038 | -9.01 |
| HT 10 h | 0.148 | 0.382 | 0.172 | 105.9 | 9.049 | 04.92 | 2.345 | -7.28 |
| HT 20 h | 0.135 | 0.274 | 0.176 | 113.7 | 1.056 | 04.33 | 1.776 | -5.99 |

**Fig. 8** Influence of HT time on the $\sigma_0$ for the nano-crystallized glass–ceramics



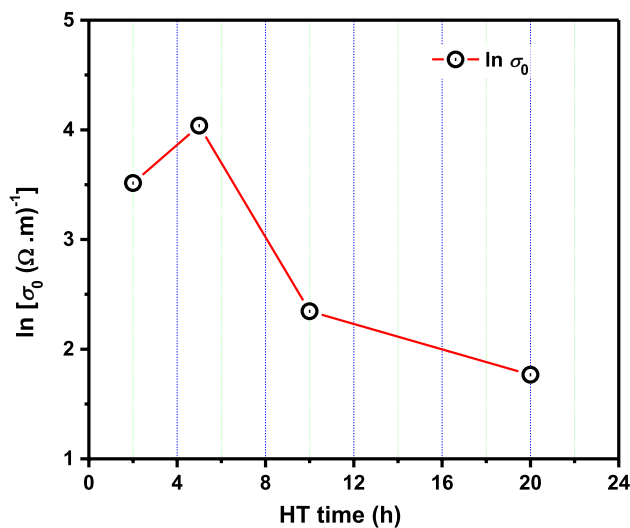**Fig. 9** The correlation between the $R$ and $W$ for the nano-crystallized glass–ceramics

the specified temperature (409 K). Figure 8 displays the influence of HT time on $\sigma_0$. This figure indicates that the $\sigma_o$ changed with HT times. Based on both of these findings, we infer that non-adiabatic SPH was responsible for the conduction mechanism in the current samples. [5].

The following formula was used to calculate the number of ions per unit volume ($N$) [43, 44]:

$$N = 2\left[\left(\frac{dP}{M}\right)N_A\right], \tag{9}$$

where $N_A$ is the Avogadro number, $P$ is the weight fraction of $V_2O_5$, $M$ is its molecular weight, and $d$ is the density. The average distance $R$ between TMIs was determined through [43, 44]:

$$R = \left(\frac{1}{N}\right)^{1/3}. \tag{10}$$

The $R$ and $N$ values for the current glass and nano-crystallized glass–ceramics are listed in Table 1.

For nano-crystallized glass–ceramics, Fig. 9 illustrates the correlation between $R$ and $W$. $W$ was affected by the site-to-site distance $R$ in the measurement range. This result demonstrated that the relationship between $W$ and $R$ was positive. This result was consistent with previous reports [16, 32]. The nano-crystallized glass–ceramic annealing for 20 h had the lowest $W$ (as presented in Fig. 9). This low $W$ could be explained by a decrease in grain boundary scattering [16].

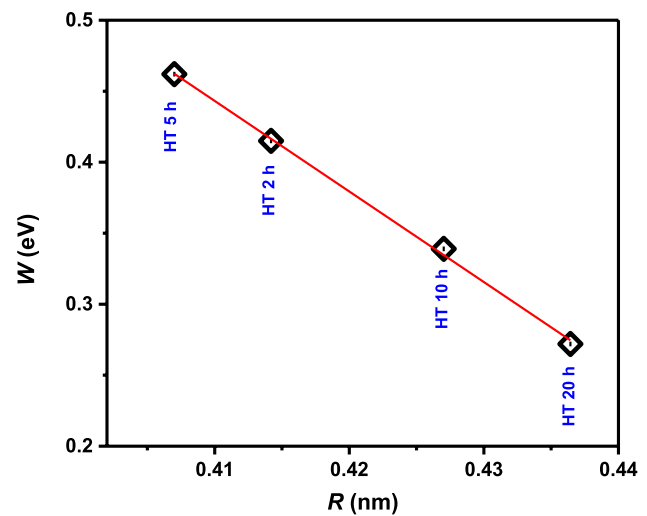The polaron radius, $r_p$, was computed using distance $R$ from the formula [5, 6]:

$$r_P = \left(\frac{\pi}{6}\right)^{1/3}\frac{R}{2}. \tag{11}$$

The $r_p$ values are included in Table 2. It has been observed that for the present glass and its nano-crystallized glass–ceramics, $r_p < R$. This indicates strong localization of the carriers in this system. The following relation was used to compute the polaron hopping energy ($W_H$) [5, 6]:

$$W_H = \frac{e^2}{4\varepsilon_P}\left(\frac{1}{r_P} - \frac{1}{R}\right), \tag{12}$$

where $\varepsilon_P$ is the effective dielectric constant.

$$\frac{1}{\varepsilon_P} = \frac{1}{\varepsilon_\infty} - \frac{1}{\varepsilon_s}, \tag{13}$$

where $\varepsilon_s$ and $\varepsilon_\infty$ are the static and high-frequency dielectric constants, respectively. $\varepsilon_s$ was recorded at 120 Hz, whereas $\varepsilon_\infty$ was recorded at 100,000 Hz [32]. The computed $W_H$ and $\varepsilon_p$ values are recorded in Table 2. To determine the density of states at the Fermi level, $N(E_F)$, the following formula could be used [6, 16, 32]:

$$N(E_F) = \frac{3}{4\pi R^3 W}. \tag{14}$$

The $N(E_F)$ values for the current glass and nano-crystallized glass–ceramics are scheduled in Table 2.

The small polaron coupling constant ($\gamma_p$), a measuring electron–phonon interaction, was obtained by utilizing the relationship [4]

$$\gamma_P = \frac{2W_H}{h\nu_0}. \tag{15}$$

The calculated values of $\gamma_p$ for the current glass and its nano-crystallized glass–ceramics are summarized in Table 2. Generally, the $\gamma_p > 4$ referred to the strong electron–phonon interaction [5].

The polaron hopping model was studied by Emin and Holstein [45]. For the case of non-adiabatic hopping, they derived an equation for the $\sigma_{dc}$:

$$\sigma_{dc} = \left(\frac{3e^2NR^2J^2}{2kT}\right)\left(\frac{\pi}{kTW_H}\right)\exp(-2\alpha R)\exp\left(-W_H/kT\right).$$

(16a)

But for the adiabatic hopping:

$$\sigma_{dc} = \left(\frac{3e^2NR^2J^2}{2kT}\right)\left(\frac{\pi}{kTW_H}\right)\exp\left(-\frac{W_H - J}{kT}\right),$$

(16b)

where $J$ denotes the polaron bandwidth associated with the overlap of the electron wave functions on the nearby sites. The nature of SPH conduction could also be examined using the polaron bandwidth, $J$, or the electron overlap integral, regardless of whether the system is adiabatic or non-adiabatic, as follows [45]:

For adiabatic

$$J > \left(\frac{2kTW_H}{\pi}\right)^{1/4}\left(\frac{\hbar\nu_0}{\pi}\right)^{1/2}.$$

(17a)

And for non-adiabatic

$$J < \left(\frac{2kTW_H}{\pi}\right)^{1/4}\left(\frac{\hbar\nu_0}{\pi}\right)^{1/2}.$$

(17b)

The values of $J$, which are estimated from the right-hand side of Eqs. (17a) or (17b), at 409 K for the current glass and nano-crystallized glass–ceramics, were found to be in the range of 0.0132–0.0165 eV. $J$ must be calculated to clearly adopt whether the polaron is in an adiabatic or non-adiabatic system, and it could be determined via [34]:

$$J \approx e^3\left[\frac{N(E_F)}{(\varepsilon_0\varepsilon_P)^3}\right]^{1/2}.$$

(18)

The $J$ values could be computed from Eq. (18) by utilizing the $N(E_F)$ and $\varepsilon_p$ values for the current glass and nano-crystallized glass–ceramics. The $J$ values obtained using Eq. (18) were approximately $J < 0.001$ eV. It can be noted that the $J$ values for the current glass and nano-crystallized glass–ceramics (calculated by Eq. (18)) were clearly less than that of the right-hand side of Eqs. (17a) or (17b). So, for the current glass and corresponding nano-crystallized glass–ceramics, the theory of non-adiabatic hopping was the best suited to explain the phenomenon of polaron transport at great temperatures. Both of the above

**Table 3** $\mu$ and $N_c$ of 18.75Li$_2$O–18.75Na$_2$O–25V$_2$S$_5$–37.5P$_2$S$_5$ glass and its nano-crystallized glass–ceramics at constant temperature (409 K)

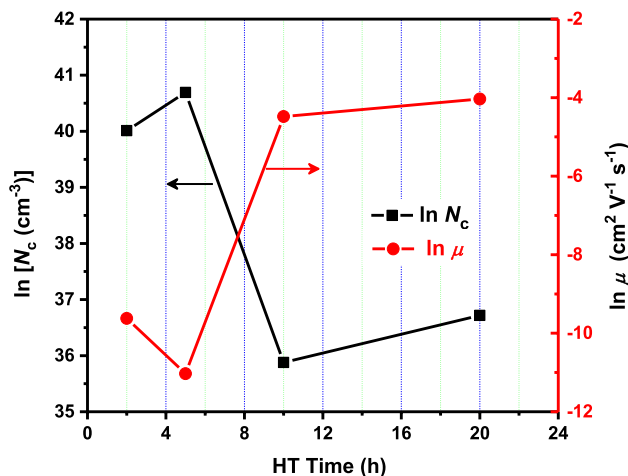| Sample | $\mu \pm 0.02$ ($\times 10^{-6}$ cm$^2$ V$^{-1}$ s$^{-1}$) | $N_c \pm 0.02$ ($\times 10^{16}$ cm$^{-3}$) |
|---|---|---|
| Glass | 32.44 | 08.52 |
| HT 2 h | 66.25 | 23.80 |
| HT 5 h | 16.22 | 47.07 |
| HT 10 h | 11,300 | 0.382 |
| HT 20 h | 17,707 | 0.883 |



**Fig. 10** Effect of HT time on the $\mu$ and $N_c$, at 409 K for the nano-crystallized glass–ceramics

outcomes indicate that the current system conduction was owing to the non-adiabatic SPH of electrons.

The hopping carrier mobility, $\mu$, in the non-adiabatic hopping system was obtained by the formula [5]:

$$\mu = \left(\frac{eR^2}{kT}\right)\left(\frac{1}{\hbar}\right)\left(\frac{\pi}{4W_HkT}\right)^{1/2}J^2\exp(-W/kT).$$

(19)

In addition, the carrier density $N_c$ was computed by the relationship [6]:

$$N_c = \frac{\sigma_{dc}}{e\mu}.$$

(20)

The $\mu$ and $N_c$ values for the current glass and nano-crystallized glass–ceramics were listed in Table 3 and Fig. 10. These values were in agreement with the values reported in the previous papers [6, 16, 28, 40]. The electrons are strongly localized at the V-ion sites due to the strong electron–phonon interaction with large $\gamma_p$ [16, 32], as evidenced by the very small of $\mu$ for the current system at 409 K. Owing to the localized condition for the conducting electrons being usual for $\mu < 0.01$ cm$^2$V$^{-1}$ s$^{-1}$, the creation of SP in the current

glass and nano-crystallized glass–ceramics was reconfirmed [5]. Furthermore, since there was no significant change in the $N_c$ values, the conductivity was principally decided by the hopping mobility [16].

The approach described by Greaves [46] as an adjustment to Molt's variable range hopping (VRH) model [47] may be used at intermediate temperature, and it gave the following formula for the $\sigma_{dc}$:

$$\sigma_{dc} T^{1/2} = A \exp\left(-\frac{B}{T^{1/4}}\right), \tag{21}$$

where $A$ and $B$ are constants. $B$ is estimated by:

$$B = 2.1 \left[\frac{\alpha^3}{N(E_F)}\right]^{1/4}. \tag{22}$$

Figure 11 illustrates $\ln(\sigma_{dc} T^{1/2})$ as a function of $T^{-1/4}$. Expression (21) provided an excellent match to the experimental data in the intermediate temperature region, indicating that Greaves' VRH might be applicable to the current glass and its nano-crystallized glass–ceramic. Table 4 contains the parameters $A$ and $B$ derived from these curves. Expression (22) was utilized to determine the factor $\alpha$. It is found that the $\alpha$ and $N(E_F)$ values were appropriate for the localized states [5, 16, 40].

## 4 Conclusions

18.75Li$_2$O–18.75Na$_2$O–25V$_2$S$_5$–37.5P$_2$S$_5$ glass and corresponding nano-crystallized glass–ceramics were successfully synthesized by utilizing melt-quenching and HT
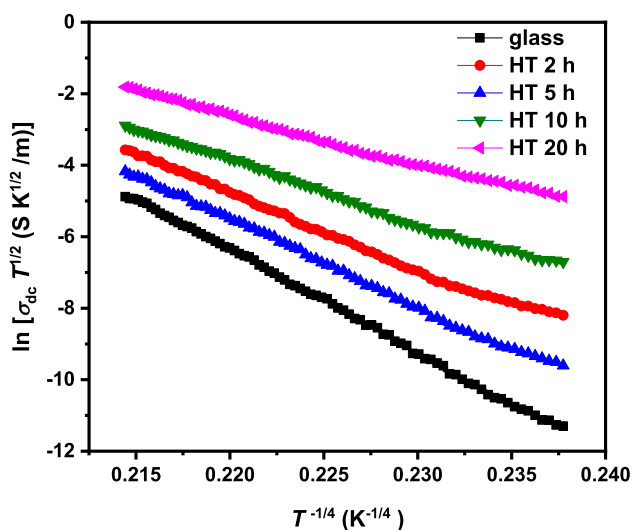
**Table 4** Parameters of Greaves VRH for 18.75Li$_2$O–18.75Na$_2$O–25V$_2$S$_5$–37.5P$_2$S$_5$ glass and its nano-crystallized glass–ceramics

| Sample | $A \pm 0.01$ [K$^{1/2}$ / Ω m] | $B \pm 0.2$ ( K$^{1/4}$) | $\alpha \pm 0.02$ ( Å$^{-1}$) |
|---|---|---|---|
| Glass | 50.11 | 258.6 | 4.72 |
| HT 2 h | 24.25 | 136.5 | 2.32 |
| HT 5 h | 34.58 | 185.9 | 3.44 |
| HT 10 h | 24.18 | 130.1 | 2.26 |
| HT 20 h | 22.04 | 113.2 | 1.98 |

techniques at 405 °C for 2, 5, 10 and 20 h. The effects of the HT time on the structural and electrical features of the nano-crystallized glass–ceramics were investigated. XRD spectrum of the as-prepared glass promoted the amorphous nature. XRD spectra of the nano-crystallized glass–ceramics revealed nanocrystallites incorporated in the glassy phase with nano-crystalline size between 37 and 50 nm. The amorphous and crystalline natures of the as-synthesized glass and nano-crystallized glass–ceramics were also verified by FESEM images. The nano-crystallized glass–ceramics demonstrated higher dc conductivity and lower activation energy for conduction than the as-prepared glass because between V$_2$O$_5$ nanoparticles there had formed a vast and dense network of electronic conductivity tracks. The conductivity and crystalline size exhibited opposite behaviors to each other (i.e., the grain boundary scattering affected electrical conductivity). The nano-crystallized glass–ceramic annealing for 20 h which had the lowest particle size, demonstrated the highest dc conductivity and the lowest activation energy. This outcome could be ascribed to the reduction in the scattering of grain boundary owing to the decrease in particle size. The conductivity was principally determined by hopping carrier mobility, and it was verified that the conduction obeyed non-adiabatic SPH. The Greaves VRH model was found to be suitable at intermediate temperatures.

**Fig. 11** $\ln(\sigma_{dc} T^{1/2})$ as a function of $T^{-1/4}$ for the glass sample and nano-crystallized glass–ceramics

## Declarations

**Conflict of interest** The authors declare no competing interest.

**Ethical approval** The work does not require ethical approval.

## References

1. M.M. El-Desoky, Small polaron transport in $V_2O_5$–NiO–$TeO_2$ glasses. J. Mater. Sci. **14**, 215–221 (2003). https://doi.org/10.1023/A:1022981929472
2. M.S. Al-Assiri, M.M. El-Desoky, Grain-size effects on the structural, electrical properties and ferroelectric behaviour of barium titanate-based glass–ceramic nano-composite. J. Mater. Sci. **24**, 784–792 (2013). https://doi.org/10.1007/s10854-012-0810-x
3. K. Fukuda, A. Ikeda, T. Nishida, A significant improvement of the electrical conductivity of semiconducting vanadate glasses caused by heat treatment. Solid State Phenom. **90–91**, 215–220 (2003). https://doi.org/10.4028/www.scientific.net/SSP.90-91.215
4. N.F. Mott, Electrons in disordered structures. Adv. Phys. **16**, 49–144 (1967). https://doi.org/10.1080/00018736700101265
5. I.G. Austin, N.F. Mott, Polarons in crystalline and non-crystalline materials. Adv. Phys. **18**, 41–102 (1969). https://doi.org/10.1080/00018736900101267
6. M.M. El-Desoky, A.M. Al-Syadi, M.S. Al-Assiri, H.M. Hassan, Effect of sulfur addition and nanocrystallization on the transport properties of lithium–vanadium–phosphate glasses. J. Mater. Sci.: Mater. Electron. **29**, 968–977 (2018). https://doi.org/10.1007/s10854-017-7994-z
7. L. Jlassi, H. Elhouichet, A comparative investigation of optical and electrical properties of vanadate zinc lithium phosphate glass and nanostructured glass–ceramics. Braz. J. Phys. **52**, 1–13 (2022). https://doi.org/10.1007/s13538-021-01005-3
8. S. Mandaland, S. Hazra, Structural and physical properties of $Fe_2O_3$-doped lead vanadate glass. J. Mater. Res. **15**, 218–221 (2000). https://doi.org/10.1557/JMR.2000.0035
9. S. Yusub, P.S. Rao, D.K. Rao, Ionic conductivity, dielectric and optical properties of lithium lead borophosphate glasses combined with manganese ions. J. Alloys and Compounds **663**, 708–717 (2016). https://doi.org/10.1016/j.jallcom.2015.12.147
10. A.M. Al-Syadi, M.S. Al-Assiri, H.M. Hassan, G. El Enany, M.M. El-Desoky, Effect of sulfur addition on the electrochemical performance of lithium-vanadium-phosphate glasses as electrodes for energy storage devices. J. Electroanal. Chem. **804**, 36–41 (2017). https://doi.org/10.1016/j.jelechem.2017.09.041
11. A.M. Al-Syadi, Electrochemical performance of $Na_2O$–$Li_2O$–$P_2S_5$–$V_2S_5$ glass–ceramic nanocomposites as electrodes for supercapacitors. Appl. Phys. A **127**, 755 (2021). https://doi.org/10.1007/s00339-021-04899-7
12. T. Honma, K. Nagamine, T. Komatsu, Fabrication of olivine-type $LiMnxFe_1-xPO_4$ crystals via the glass–ceramic route and their lithium ion battery performance. Ceram. Int. **36**, 1137–1141 (2010). https://doi.org/10.1016/j.ceramint.2009.10.003
13. S.J. Japari, A.K. Yahya, R. Hisam, Effects of mixed-alkali oxides on AC conductivity and dielectric properties of $xNa_2O$–(20–x)$K_2O$–$30V_2O_5$–$50TeO_2$ glasses. Results Phys. **16**, 102905 (2020). https://doi.org/10.1016/j.rinp.2019.102905
14. J.E. Garbarczyk, P. Jozwiak, M. Wasiucionek, J.L. Nowinski, Enhancement of electrical conductivity in lithium vanadate glasses by nanocrystallization. Solid State Ionics **175**, 691–694 (2004). https://doi.org/10.1016/j.ssi.2004.08.025
15. J.E. Garbarczyk, P. Jozwiak, M. Wasiucionek, J.L. Nowinski, Nanocrystallization as a method of improvement of electrical properties and thermal stability of $V_2O_5$-rich glasses. J. Power Sources **173**, 743–747 (2007). https://doi.org/10.1016/j.jpowsour.2007.05.069
16. A.M. Al-Syadi, M.S. Al-Assiri, H.M. Hassan, M.M. El-Desoky, Grain size effects on the transport properties of $Li_3V_2(PO_4)_3$ glass–ceramic nanocomposites for lithium cathode batteries. J. Mater. Sci.: Mater. Electron. **27**, 4074–4083 (2016). https://doi.org/10.1007/s10854-015-4266-7
17. M.Y. Murashkin, I. Sabirov, X. Sauvage, R.Z. Valiev, Nanostructured Al and Cu alloys with superior strength and electrical conductivity. J. Mater. Sci. **51**, 33–49 (2016). https://doi.org/10.1007/s10853-015-9354-9
18. A. Gupta, V. Choudhary, Electrical conductivity and shielding effectiveness of poly(trimethylene terephthalate)/multiwalled carbon nanotube composites. J. Mater. Sci. **46**, 6416–6423 (2011). https://doi.org/10.1007/s10853-011-5591-8
19. S.A. Abdelwahab, A. Ali, K. Abdelwahed, I. Ahmed, A.I. Ali, Influence of $TiO_2$/GO weight ratio on the structure, mechanical, and electrical properties of $SiO_2$–$Al_2O_3$ glass–ceramics. J. Mater. Sci.: Mater. Electron. **32**, 11092–11106 (2021). https://doi.org/10.1007/s10854-021-05774-0
20. P. Jozwiak, J.E. Garbarczyk, Mixed electronic–ionic conductivity in the glasses of the $Li2O$–$V2O5$–$P2O5$ system. Solid State Ionics **176**, 2163–2166 (2005). https://doi.org/10.1016/j.ssi.2004.06.028
21. C. Cao, Z.-B. Li, X.-L. Wang, X.-B. Zhao, W.-Q. Han, Recent advances in inorganic solid electrolytes for lithium batteries. Front. Energy Res. **2**, 25 (2014). https://doi.org/10.3389/fenrg.2014.00025
22. R. Barik, P.P. Ingole, Challenges and prospects of metal sulfide materials for supercapacitors. Curr. Opin. Electrochem. **21**, 327–334 (2020). https://doi.org/10.1016/j.coelec.2020.03.022
23. L.C.R. Schneider, C.L. Martin, Y. Bultel, D. Bouvard, E. Siebert, Discrete modelling of the electrochemical performance of SOFC electrodes. Electrochim. Acta **52**, 314–324 (2006). https://doi.org/10.1016/j.electacta.2006.05.018
24. C.W. Kim, J.S. Park, K.S. Lee, Effect of $Fe_2P$ on the electron conductivity and electrochemical performance of $LiFePO_4$ synthesized by mechanical alloying using Fe3+ raw material. J. Power Sources **163**, 144–150 (2006). https://doi.org/10.1016/j.jpowsour.2006.02.071
25. S. Kumar, B. Kishore, N. Munichandraiah, Electrochemical studies of non-aqueous Na–$O_2$ cells employing Ag-RGO as the bifunctional catalyst. RSC Adv. **6**, 63477–63479 (2016). https://doi.org/10.1039/C6RA13596J
26. A.M. Al-Syadi, M.S. Al-Assiri, H.M. Hassan, M.M. El-Desoky, Grain size effects on dynamics of Li-ions in $Li_3V_2(PO_4)_3$ glass-ceramic nanocomposites. Ionics **22**, 2281–2290 (2016). https://doi.org/10.1007/s11581-016-1772-4
27. V.D. Mote, Y. Purushotham, B.N. Dole, Williamson-Hall analysis in estimation of lattice strain in nanometer-sized ZnO particles. J. Theor. Appl. Phys. **6**, 1–8 (2012). https://doi.org/10.1186/2251-7235-6-6
28. A.E. Harby, A.E. Hannora, M.S. Al-Assiri, M.M. El-Desoky, Correlation between grain size and transport properties of lead titanate based-glass–ceramic nano-composites. J. Mater. Sci.: Mater. Electron. **27**, 8446–8454 (2016). https://doi.org/10.1007/s10854-016-4859-9
29. A.A. Bahgat, Sh. Heikal, I.A. Mahdy, A.S. Abd-Rabo, A.A. Ghany, Cyclic electrical conductivity in $BaTiO_3$–$PbTiO_3$–$V_2O_5$ glass-ceramic nanocomposite. Physica B **447**, 23–29 (2014). https://doi.org/10.1016/j.physb.2014.04.048
30. E.N. Brown, P.J. Rae, D.M. Dattelbaum, B. Clausen, D.W. Brown, In-situ measurement of crystalline lattice strains in polytetrafluoroethylene. Exp. Mech. **48**, 119–131 (2008). https://doi.org/10.1007/s11340-007-9075-3

31. T. Takada, S.F. Wang, S. Yoshikawa, S.J. Jang, R.E. Newnham, Effect of glass additions on BaO–TiO$_2$–WO$_3$ microwave ceramics. J. Am. Ceram. Soc. **77**, 1909–1916 (1994). https://doi.org/10.1111/j.1151-2916.1994.tb07070.x

32. A.A. Bahgat, M.G. Moustafa, E.E. Shaisha, Enhancement of electric conductivity in transparent glass–ceramic nanocomposites of Bi$_2$O$_3$–BaTiO$_3$ glasses. J. Mater. Sci. Technol. **29**, 1166–1176 (2013). https://doi.org/10.1016/j.jmst.2013.08.005

33. Y.G. Wang, S.P. Lau, H.W. Lee, S.F. Yu, B.K. Tay, X.H. Zhang, H.H. Hng, Photoluminescence study of ZnO films prepared by thermal oxidation of Zn metallic films in air. J. Appl. Phys. **94**, 354–358 (2003). https://doi.org/10.1063/1.1577819

34. N.F. Mott, Conduction in glasses containing transition metal ions. J. Non-Cryst. Solids **1**, 1–17 (1968). https://doi.org/10.1016/0022-3093(68)90002-1

35. J.E. Garbarczyk, T.K. Pietrzak, M. Wasiucionek, A. Kaleta, A. Dorau, J.L. Nowiński, High electronic conductivity in nanostructured materials based on lithiumiron-vanadate-phosphate glasses. Solid State Ionics **272**, 53–59 (2015). https://doi.org/10.1016/j.ssi.2014.12.019

36. T.K. Pietrzak, E. Jerzye, M. Wasiucionek, J.L. Nowiński, Nanocrystallisation in vanadate phosphate and lithium iron vanadate phosphate glasses. Phys. Chem. Glasses-Eur. J. Glass Sci. Technol. Part B **57**, 113–124 (2016). https://doi.org/10.13036/17533562.57.3.038

37. T.K. Pietrzak, J.E. Garbarczyk, I. Gorzkowska, M. Wasiucionek, J.L. Nowinski, S. Gierlotka, P. Jozwiak, Correlation between electrical properties and microstructure of nanocrystallized V$_2$O$_5$–P$_2$O$_5$ glasses. J. Power Sources **194**, 73–80 (2009). https://doi.org/10.1016/j.jpowsour.2009.02.031

38. M.S. Al-Assiri, M.M. El-Desoky, Correlation between nanostructural and electrical properties of barium titanate-based glass–ceramic nano-composites. J. Alloy. Compd. **509**, 8937–8943 (2011). https://doi.org/10.1016/j.jallcom.2011.06.079

39. M.Y. Hassaan, F.M. Ebrahim, A.G. Mostafa, M.M. El-Desoky, Effect of sulfur addition and heat treatment on electrical conductivity of barium vanadate glasses containing iron. Mater. Chem. Phys. **129**, 380–384 (2011). https://doi.org/10.1016/j.matchemphys.2011.04.029

40. M.S. Al-Assiri, S.A. Salem, M.M. El-Desoky, Effect of iron doping on the characterization and transport properties of calcium phosphate glassy semiconductors. J. Phys. Chem. Solids **67**, 1873–1881 (2006). https://doi.org/10.1016/j.jpcs.2006.04.015

41. N.F. Mott, Conduction in non-crystalline materials: III. Localized states in a pseudogap and near extremities of conduction and valence bands. Philos. Mag. **19**, 835–852 (1969). https://doi.org/10.1080/14786436908216338

42. H.H. Qiu, H. Sakata, T. Hirayama, Electrical conductivity of Fe$_2$O$_3$-PbO-Bi$_2$O$_3$ glasses. J. Ceram. Soc. Jpn. **104**, 1004–1007 (1996). https://doi.org/10.2109/jcersj.104.1004

43. M. Pant, D.K. Kanchan, P. Sharma, M.S. Jayswal, Mixed conductivity studies in silver oxide based barium vanado–tellurite glasses. Mater. Sci. Eng., B **149**, 18–25 (2008). https://doi.org/10.1016/j.mseb.2007.11.037

44. H. Mori, T. Kitami, H. Sakata, Electrical conductivity of V2O5-Sb2O3- TeO2 glasses. J. Non-Cryst. Solids **168**, 157–166 (1994). https://doi.org/10.1016/0022-3093(94)90132-5

45. D. Emin, T. Holstein, Studies of small-polaron motion IV. Adiabatic theory of the Hall Effect. Ann. Phys. **53**, 439–520 (1969). https://doi.org/10.1016/0003-4916(69)90034-7

46. G.N. Greaves, Small polaron conduction in V$_2$O$_5$ P$_2$O$_5$ glasses. J. Non-Cryst. Solids **11**, 427–446 (1973). https://doi.org/10.1016/0022-3093(73)90089-6

47. N.F. Mott, E.A. Davis, *Electronic Processes in Non-crys-talline Materials* (Oxford University Press, Oxford, 2012)